

## Massive Young Stellar Objects and Outflow in the Infrared-Dark Cloud G79.3+0.3

ANNA S.E. LAWS,<sup>1,2</sup> JOSEPH L. HORA,<sup>3</sup> AND QIZHOU ZHANG<sup>3</sup>

<sup>1</sup>*Astrophysics Group, University of Exeter, Stocker Road, Exeter, EX4 4QL, U.K.*

<sup>2</sup>*School of Physics and Astronomy, University of Southampton, Highfield, Southampton SO17 1BJ, UK*

<sup>3</sup>*Center for Astrophysics | Harvard & Smithsonian, 60 Garden Street, Cambridge, MA 02138, USA*

### ABSTRACT

G79.3+0.3 is an infrared-dark cloud (IRDC) in the Cygnus-X complex that is home to massive deeply-embedded Young Stellar Objects (YSOs). We have produced a Submillimeter Array (SMA) 1.3 mm continuum image and <sup>12</sup>CO line maps of the eastern section of G79.3+0.3 in which we detect five separate YSOs. We have estimated physical parameters for these five YSOs and others in the vicinity of G79.3+0.3 by fitting existing photometry from *Spitzer*, *Herschel*, and ground-based telescopes to spectral energy distribution (SED) models. Through these model fits we find that the most massive YSOs seen in the SMA 1.3 mm continuum emission have masses in the 5 – 6  $M_{\odot}$  range. One of the SMA sources was observed to power a massive collimated <sup>12</sup>CO outflow extending at least 0.94 pc in both directions from the protostar, with a total mass of 0.83  $M_{\odot}$  and a dynamical timescale of 23 kyr.

*Keywords:* stars: formation – stars: massive – ISM: general – ISM: clouds – ISM: structure – ISM: individual objects: G79.3+0.3

### 1. INTRODUCTION

Massive stars are known to form in clusters in dense molecular clouds, but there are several aspects of the formation process that are not well-understood. For example, it is not yet known which is the dominant massive star formation mechanism (i.e., monolithic collapse, competitive accretion, and stellar collisions and mergers; e.g. see reviews by Zinnecker & Yorke 2007; McKee & Ostriker 2007; Tan et al. 2014; Motte et al. 2017). In order to determine the critical processes involved, it is necessary to find and study examples of massive stars in various stages of formation. This task is made difficult by the relatively short formation period and lifetime of massive stars, the low numbers of massive stars given by the mass function of stellar clusters, and the fact that the birthplace of these stars are in the cores of dense molecular clouds, making the massive Young Stellar Objects (YSOs) difficult to observe.

With the availability of sensitive infrared surveys from the *Spitzer* Space Telescope (Werner et al. 2004), and high-resolution (sub)millimeter interferometers such as the Submillimeter Array (SMA), it is possible to probe these deeply-embedded YSOs near the beginning of their formation pro-

cess. Several investigations have identified and studied the objects known as infrared dark clouds (IRDCs), which have been often found to host sites of massive star formation (e.g. Wang et al. 2006; Rathborne et al. 2006; Cyganowski et al. 2008; Peretto & Fuller 2010). The SMA has been used to study young massive embedded clusters, revealing information on the earliest stages of formation and mass accretion (e.g., Zhang et al. 2009; Zhang & Wang 2011; Wang et al. 2013, 2014). By combining the IR and submm data, we can study the formation of YSOs and the cluster from its earliest stages onward.

Cygnus-X is one of the most massive molecular cloud complexes in the Galaxy with a total mass of  $3 \times 10^6 M_{\odot}$  (Schneider et al. 2006), and is one of the nearest massive star-forming complexes at a distance of  $1.40 \pm 0.08$  kpc (Rygl et al. 2012). Along with YSOs, Cygnus-X includes 800 distinct H II regions (evidence of widespread massive star formation), several OB associations, and several Wolf-Rayet and O3 stars (Beerer et al. 2010). The Cygnus OB2 star cluster contains hundreds of massive OB and O stars, with a stellar mass of  $\sim 1.7 \times 10^4 M_{\odot}$  (Wright et al. 2015). Altogether this makes the complex an excellent target for observing massive stars and their formation.

In this paper, we study a region in the IRDC G79.3+0.3 (Carey et al. 1998; Redman et al. 2003, see Figure 1). This IRDC is one of the largest in the Cygnus-X region, and lies in the central subsection of Cygnus-X near DR15, an H II region

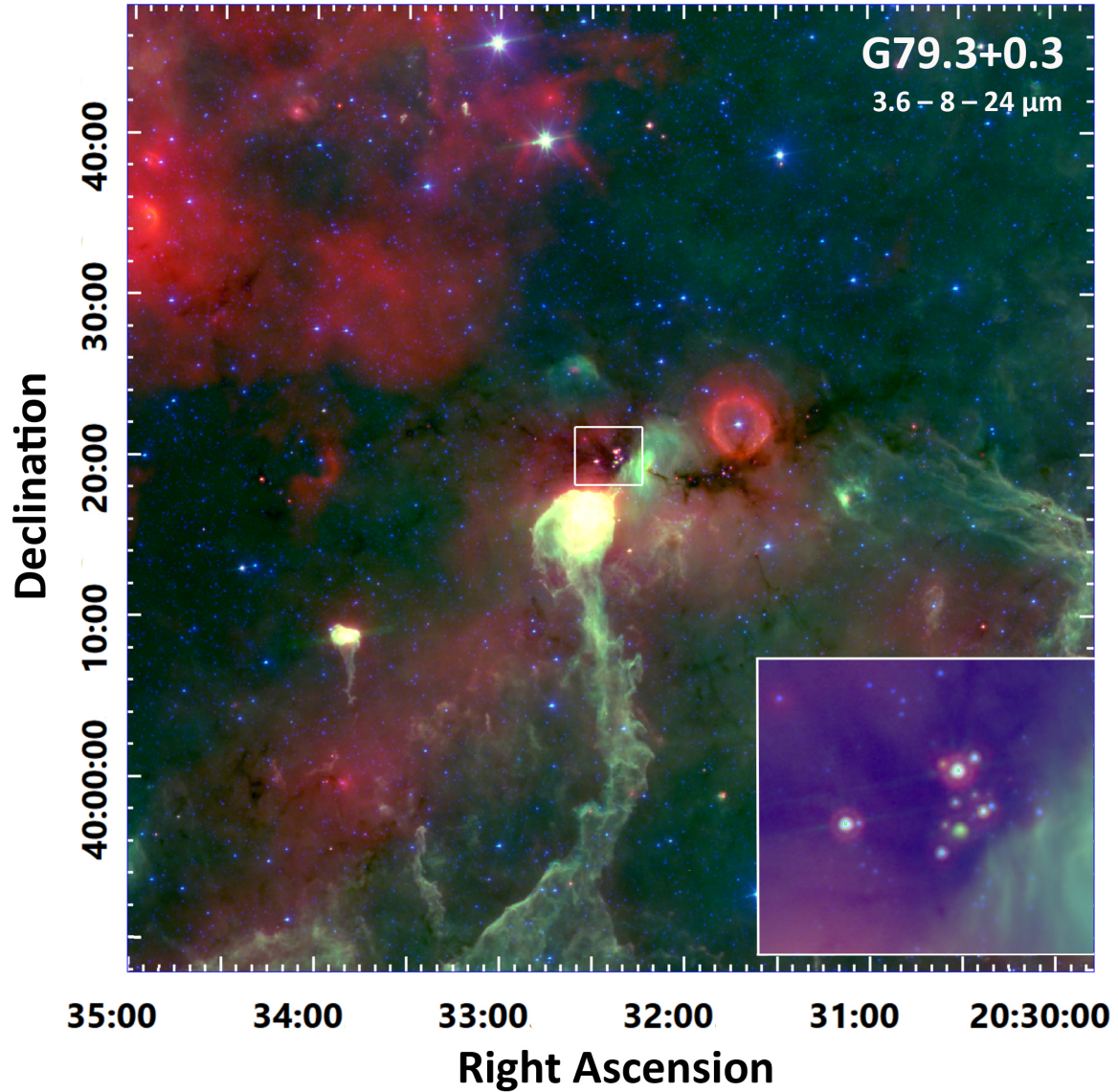


**Figure 1.** A near-IR view of the G79.3+0.3 and its surroundings. The region in G79.3+0.3 observed with the SMA is directly in the center of this image, highlighted with a white square that is enlarged within the inset. The inset shows the more immediate surroundings of the region of the IRDC imaged with the SMA, spanning about  $3.7 \times 3.0$  arcmin or  $1.5 \times 1.2$  pc. The IRDC can be seen as the dark area immediately surrounding the central YSOs, continuing to the top and left sides of the inset. These are composite images using three wavebands,  $3.6 \mu\text{m}$  (blue),  $8 \mu\text{m}$  (green), and  $24 \mu\text{m}$  (red) from the *Spitzer* Space Telescope.

that has been previously targeted as a candidate for high-mass star formation (Rivera-Gálvez et al. 2015; Schneider et al. 2016). Star formation is especially promising in DR15 with its molecular pillar and prominent bright envelope (as seen in Figure 1), though the IRDC is likely not interacting with the pillar (Rivera-Gálvez et al. 2015). Located close to the IRDC is the luminous blue variable (LBV) candidate star G79.29+0.46, seen as the blue star in the middle of the circular red nebula to the right of center in Figure 1. Studies by Umama et al. (2011) with the EVLA and observations of  $\text{NH}_3$  (1, 1) and (2, 2) emission by Rizzo et al. (2014) showed evidence that the LBV is interacting with the IRDC. Following Rizzo

et al. (2014), we assume that the IRDC G79.3+0.3 is located at the same distance as Cygnus-X at 1.4 kpc.

A total of 226 young stellar sources have previously been seen in the DR15 area, and the Class 0 and I objects are mostly intermediate- to high-mass stars (Rivera-Gálvez et al. 2015). G79.3+0.3 has a molecular mass of  $803 M_\odot$ , which is average for the sample of 45 massive star-forming IRDCs given in Ragan et al. (2012), but high compared with the other Cygnus-X IRDCs (Calahan et al., in prep.) thus making the cloud a likely location of massive YSOs in Cygnus-X. G79.3+0.3 is much closer than most IRDCs, at a distance of 1.4 kpc compared with the mean distance to classical IRDCs

of  $>3$  kpc (Ragan et al. 2012), giving a greatly improved chance of resolving individual objects within the cloud.

YSOs can produce molecular outflows as a consequence of the accretion process. As protostars gain mass through accretion, infalling gas with excess angular momentum is ejected in a wind (Shu et al. 2000; Shang et al. 2007) that accelerates the ambient material to higher velocities seen as molecular outflows in CO and SiO (e.g. Lee et al. 2002; Palau et al. 2006; Zhang et al. 1995). Surveys of massive star forming regions (Zhang et al. 2001, 2005; Beuther et al. 2002) revealed ubiquitous outflows associated with massive protostars. The mass, momentum and energy are typically orders of magnitude larger than those of the low mass stars. These studies provided crucial observational constraints on the formation process of massive stars. In more recent years, outflows and H<sub>2</sub>O masers were also detected in massive IRDC clumps (Wang et al. 2006, 2012, 2014), indicative of star forming activities in these clouds. Thanks to the physical connections with accretion, outflow energetics provide valuable insights into the accretion process of protostars.

In this paper we present the results of our study of the YSOs in G79.3+0.3, including new high-resolution SMA interferometric observations of a portion of the G79.3+0.3 IRDC. In Section 2 we provide the details of the new observations, and also describe the photometry we used from the *Spitzer* and *Herschel* missions and from ground-based near-IR surveys. Section 3 gives the results of our SED modelling of YSOs. The analysis of the outflow detected in SMA source 1 is described in Section 4, along with discussion of former studies of these objects. We summarize the main findings in Section 5.

## 2. OBSERVATIONS AND DATA REDUCTION

### 2.1. SMA

The Submillimeter Array<sup>1</sup> (Ho et al. 2004) is an interferometer consisting of eight 6 m-diameter antennas operating at millimeter and sub-millimeter wavelengths located near the summit of Maunakea, Hawaii. The SMA observations of G79.3+0.3 were carried out on July 8th 2012 and August 3rd 2012 using the Compact and Subcompact array configurations respectively. The array used the 230 GHz receivers tuned to an LO frequency of 224.92 GHz. With an IF frequency of 4 to 8 GHz the observations covered sky frequencies of 216.9 – 220.9 GHz in the lower sideband (LSB) and 228.9 – 232.9 GHz in the upper sideband (USB). The digital correlator was configured to a uniform spectral resolution of 0.8 MHz per spectral channel across the entire 8 GHz band.

<sup>1</sup>The Submillimeter Array is a joint project between the Smithsonian Astrophysical Observatory and the Academia Sinica Institute of Astronomy and Astrophysics and is funded by the Smithsonian Institution and the Academia Sinica.

The FWHM of the primary beam response of the 6 m antennas is approximately  $55''$ . The observations employed a total of 10 pointings separated by half of the FWHM of the primary beam. We used MWC349A and QSO 2007+404 as the time dependent gain calibrators. The spectral bandpass was calibrated using 3C279. The flux calibration was carried out through observations of a known flux source Titan. The uncertainty of the absolute flux calibration is about 15%. The system temperatures during the observations were from 120 to 160 K.

We calibrated the data using the MIR software (Millimeter Interferometer Reduction)<sup>2</sup> following the procedure outlined at the SMA data reduction website. The calibrations include systemic temperature correction, bandpass, time dependent gain variations, and flux calibration. The calibrated visibilities were then exported to MIRIAD and CASA for imaging. We separated the continuum and line emission in visibilities and then Fourier transformed and cleaned. We used *tclean* task in CASA with Briggs weighting and a robust parameter of 0.5. The resulting 1.3 mm continuum image has a  $1\sigma$  rms noise level of  $4 \text{ mJy beam}^{-1}$ . The  $1\sigma$  rms in the  $1 \text{ km s}^{-1}$  channels is  $140 \text{ mJy beam}^{-1}$ . The spatial resolution of the continuum image is approximately  $2''.5$  FWHM.

### 2.2. Infrared Photometry

We used four photometry catalogs in our study of Cygnus-X. The first contained photometry from the following infrared surveys: 2MASS (Skrutskie et al. 2006), UKIDSS (Dye et al. 2006), and *Spitzer* (Hora et al. 2011). The catalogs contain over three million objects in the region, of which we classified 30,902 as YSOs (Classes 0, I and II) using the methods described by Gutermuth et al. (2008). There are 28 objects classified as YSOs in the field observed by the SMA. For the J, H, and K bands, we used data from the two ground-based surveys UKIDSS and 2MASS. The UKIDSS survey has better resolution than 2MASS ( $\sim 1''$  vs.  $4''$ , respectively) but is saturated for objects brighter than 11 mag, so we used 2MASS data for recorded magnitudes below 11 mag and UKIDSS data otherwise. The IRAC images have FWHM resolutions of  $1''.66$ ,  $1''.72$ ,  $1''.88$ , and  $1''.98$  for the 3.6, 4.5, 5.8, and  $8 \mu\text{m}$  bands, respectively (Fazio et al. 2004). The MIPS instrument has a  $24 \mu\text{m}$  resolution of  $6''$  (Rieke et al. 2004).

We utilized *Herschel* data from three separate catalogs, one containing photometry for 579 YSOs in Cygnus-X detected by both *Spitzer* and *Herschel*/SPIRE at 250, 350, and  $500 \mu\text{m}$  (Kirk 2014). We also downloaded data from two catalogs containing photometry for 698 YSOs in Cygnus-X observed with the PACS 70 and  $160 \mu\text{m}$  bands (Marton et al. 2017). The spatial resolution of *Herschel* is approximately

<sup>2</sup><https://www.cfa.harvard.edu/~cqi/mircook.html>

**Table 1.** Fluxes and masses for the 1.3 mm sources

SMA ID	R.A. (J2000.0)	Dec.	Flux density (mJy)	Mass ( $M_{\odot}$ )
1	20:32:22.1	40:20:17.1	$65.7 \pm 1.2$	2.36
2	20:32:22.0	40:20:09.7	$128 \pm 2$	4.60
3	20:32:21.4	40:20:14.1	$150 \pm 1$	5.39
4	20:32:28.6	40:19:41.6	$61.6 \pm 0.8$	2.21
5	20:32:23.0	40:19:22.7	$39.0 \pm 0.4$	1.40

5'', 13'', 18'', 25'', and 36'' for the 70, 160, 250, 350, and 500  $\mu\text{m}$  bands, respectively.

### 3. RESULTS

#### 3.1. SMA Continuum

A comparison of G79.3+0.3 at different wavelengths is shown in Figure 2, with the new SMA 1.3 mm continuum image shown in the lower right panel. Five distinct continuum peaks (labeled SMA objects 1 through 5) can be seen, and each object's position and flux is given in Table 1. The position of SMA sources 1, 4, and 5 are indicated by crosses overlaid on the *Spitzer* and *Herschel* images in Figure 2. Two of these objects (labeled 2 and 3) show extended emission coinciding with molecular outflows. We will explore outflows identified in the CO emission in Section 3.3.

The continuum flux measurements can be used to calculate the mass of the gas surrounding the objects following the method in Motte et al. (2007, eqn.1). We assumed values of dust emissivity  $\kappa_{1.3\text{mm}} = 0.01 \text{ cm}^2 \text{ g}^{-1}$ ,  $T_{\text{dust}} = 15\text{K}$ , and a gas-to-dust mass ratio of 100:1. The masses are given in Table 1. Following Motte et al., we note that the mass estimates are uncertain by a factor of 2 due to uncertain dust emissivity. The individual masses can vary by  $\pm 30\%$  relative to each other when dust temperatures vary from 15 to 25 K, or by  $\pm 50\%$  for the 10 to 20 K temperature range.

Using the assumed distance to G79.3+0.3 of  $1.4 \pm 0.08 \text{ kpc}$ , the largest project separation between SMA objects is 0.76 pc between objects 3 and 4, and the smallest separation is 0.069 pc between 1 and 3. Objects 1, 4 and 5 form a triangle with roughly equal side lengths. The separations are: 1–4, 0.70 pc; 4–5, 0.58 pc; and 1–5, 0.38 pc, all with uncertainties on the order of  $\pm 10\%$ .

#### 3.2. SED Modeling

We used SEDFitter<sup>3</sup> v1.0 (Robitaille et al. 2007) to fit model YSO SEDs to each object's photometry and return

an estimate of its physical parameters, including mass and luminosity. It is necessary to find the object parameters by comparing observations with models as direct observational methods cannot distinguish features such as the separate central object, disc, and envelope. For objects with multiple model fits, we selected the best fit as that with the lowest chi-square value and derived object parameters from that fit. The two constraints fed into the SEDFitter are the distance to the object  $1.3 \leq d \leq 1.5 \text{ kpc}$  and the range of extinctions  $5.0 \leq A_v \leq 100 \text{ mag}$ . We created a custom filter to incorporate the SMA photometry with SEDFitter following the documentation (Robitaille 2013). The atmospheric transmission at the SMA is 100% in the frequency ranges covered by both upper and lower sidebands (Welch 1988), so the filter uses a simple function with 100% transmittance in these frequency ranges and 0% outside.

Most YSOs in the *Spitzer* catalog have no detection at the longer PACS and/or SPIRE wavelengths, constraining these objects to have a flux below a certain sensitivity limit at these wavelengths. We estimated these limits in Cygnus-X using a histogram of the number of objects measured with various fluxes. The upper limits for undetected sources are as follows: 223 and 827 mJy for the PACS 70 and 160  $\mu\text{m}$  bands respectively; and 3000, 6000, and 4000 mJy for the SPIRE 250, 350, and 500  $\mu\text{m}$  bands respectively. We similarly estimated a sensitivity limit for the SMA observations by assuming that the limit was 10% of the flux of the faintest distinct object. For SMA object 5 at flux 39.0 mJy, this gave a sensitivity limit of 3.90 mJy.

We used SEDFitter to fit all of the YSOs identified in the Cygnus-X region using color-color and color-magnitude relations (Beerer et al. 2010); the fluxes for the objects are given in Table 2. The SEDFitter results for the 28 YSOs within the region observed by the SMA are given in Table 3. The SED fitting results for the whole of Cygnus-X will be discussed in a later paper.

The SEDs of SMA objects 1, 4, and 5 are shown in Figure 3. The data points shown are from the near-IR, *Spitzer*, *Herschel*, and SMA. Where the source is not detected in the *Herschel* SPIRE bands, upper limits were used, indicated by the downward-pointed triangle symbols. Where the source was not separately resolved in the *Herschel* bands (such as SMA sources 1, 2, and 3), an upper limit based on the flux for all sources combined was used in the fitting process. For SMA source 1, we used the flux values given in the MIPS 24  $\mu\text{m}$  catalog as an upper limit due to multiple sources present. The models have discontinuities in flux at wavelengths above 200  $\mu\text{m}$  (e.g., see the left panel of Figure 3) since the signal-to-noise ratio in the models becomes poor above 100  $\mu\text{m}$  and the median uncertainty in the model fit is above 20% at millimeter wavelengths (Robitaille et al. 2006). Two of the SMA sources each have only one valid fit, likely because the

<sup>3</sup><https://github.com/astrofrog/sedfitter>

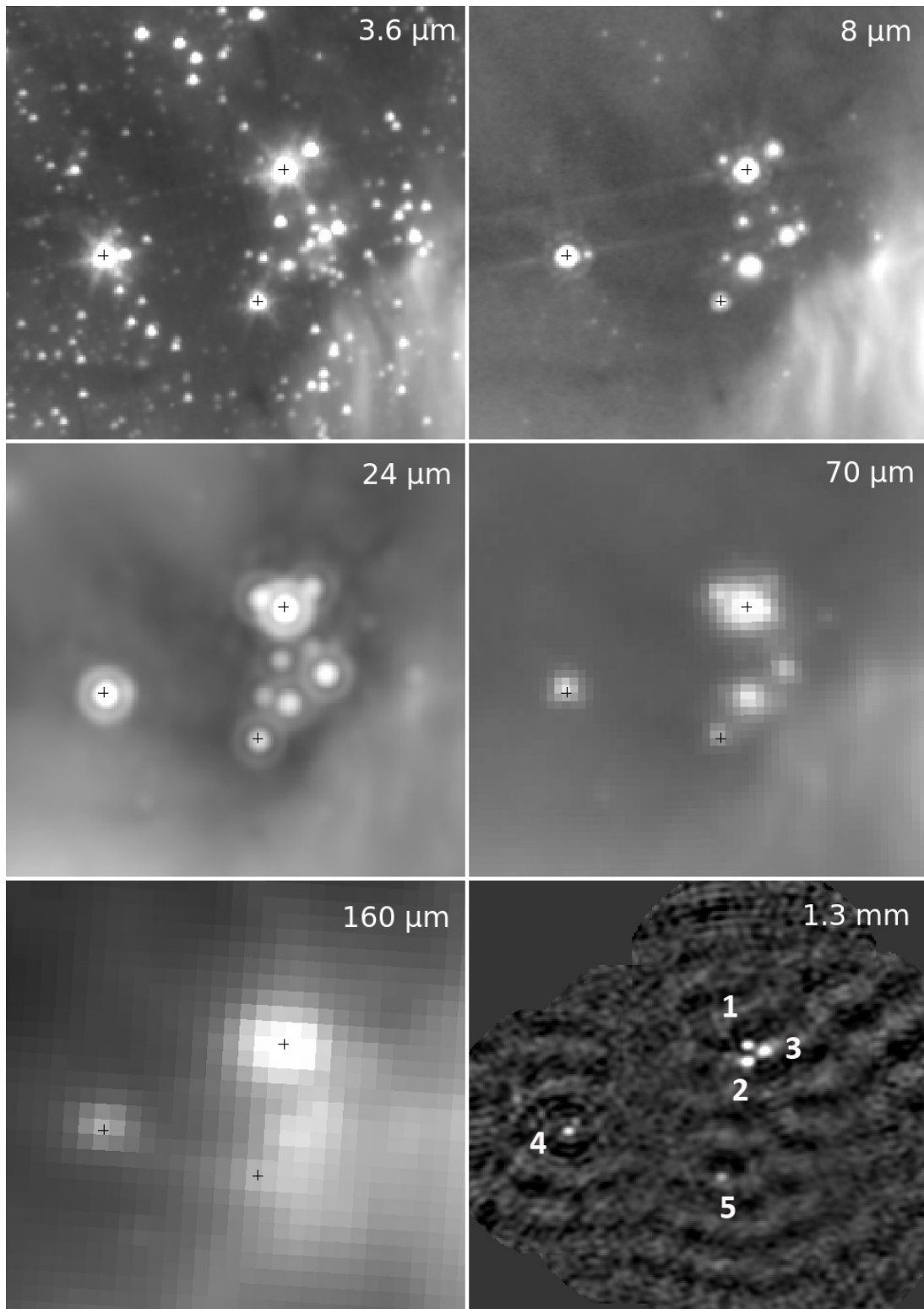


**Figure 2.** Views of G79.3+0.3 as seen in various infrared wavelengths and by the SMA. The same  $3.4' \times 3'$  region is shown in each panel. In the lower right panel the SMA image is shown with each of the continuum sources labeled. The positions of these sources are given in Table 1. The SMA objects 1, 4, and 5 (marked with the crosses in the five other panels) are each clearly visible in every image up to and including the PACS  $160 \mu\text{m}$  image. The SMA sources 2 and 3 are not detected at wavelengths shorter than  $70 \mu\text{m}$ . At 70 and  $160 \mu\text{m}$ , evidence for SMA sources 2 and 3 is present but they are not fully resolved because of the lower spatial resolution at these wavelengths.

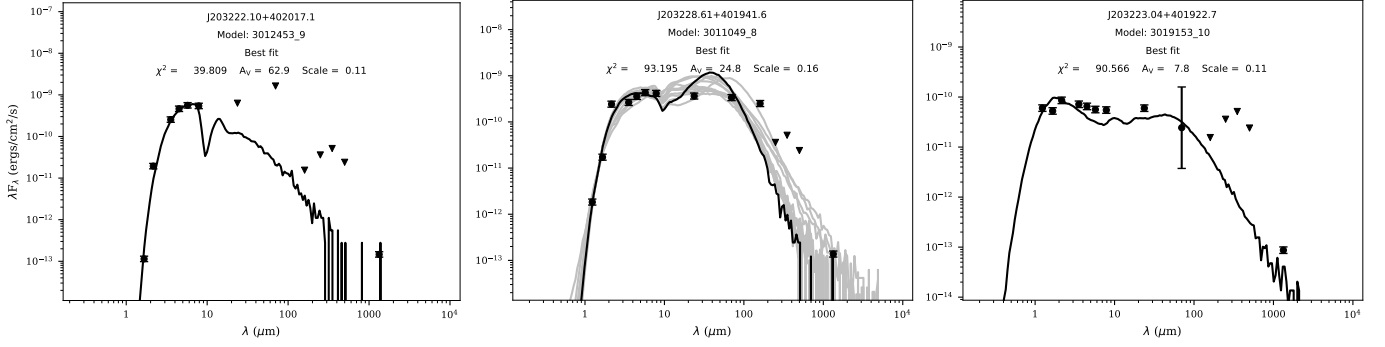


**Figure 3.** SEDs and the best model fit for SMA objects 1 (left), 4 (middle), and 5 (right). Round markers with error bars are flux measurements and their uncertainties, and downward-pointing triangles are upper limits for flux. Parameters derived from these SEDs are given in Table 3.

**Table 2.** Fluxes for 28 YSOs in the SMA-observed Region of G79.3+0.3

Name	R.A.		Decl.		Flux Density and Uncertainty (Jy)							
	(J2000.0)	(J2000.0)	<i>J</i>	<i>J</i> err	<i>H</i>	<i>H</i> err	<i>K</i>	<i>K</i> err	3.6	3.6 err		
J203222.10+402017.1	308.092102	40.338074	...	...	1.801E+01	8.408E-02	1.167E+01	9.740E-04	7.411E+00	3.000E-03		
J203228.61+401941.6	308.119202	40.328213	1.580E+01	5.838E-03	1.256E+01	8.420E-04	8.943E+00	1.600E-02	7.372E+00	3.000E-03		
J203223.04+401922.7	308.096008	40.322975	1.202E+01	6.110E-04	1.135E+01	4.000E-04	1.007E+01	1.400E-02	8.789E+00	2.000E-03		
J203220.60+401950.1	308.085846	40.330597	...	...	...	...	1.722E+01	9.206E-02	1.023E+01	1.500E-02		
J203222.25+401955.8	308.092682	40.332169	...	...	1.483E-01	2.225E-02	2.121E+00	3.181E-01	1.447E+01	2.171E+00		
J203227.86+401942.3	308.116089	40.328426	3.283E-02	4.924E-03	6.284E-01	9.426E-02	4.560E+00	6.840E-01	1.679E+01	2.518E+00		
J203221.13+402025.6	308.088043	40.340446	...	...	1.310E-01	1.964E-02	4.769E+00	7.153E-01	5.447E+01	8.170E+00		
J203220.14+401953.5	308.083893	40.331524	...	...	...	...	7.542E-01	1.131E-01	2.955E+01	4.432E+00		
J203221.13+402000.9	308.088013	40.333580	...	...	...	...	1.503E-01	1.503E-01	4.501E+00	6.752E-01		
J203227.61+401914.5	308.115021	40.320698	...	...	2.947E-01	4.421E-02	1.975E+00	2.962E-01	4.053E+00	6.079E-01		
	4.5	4.5 err	5.8	5.8 err	8	8 err	24	24 err	70	70 err	100	100 err
	6.021E+00	2.000E-03	5.066E+00	1.000E-03	4.136E+00	1.000E-03	3.950E-01	1.000E-02	...	4.431E+02	...	...
	6.304E+00	2.000E-03	5.349E+00	1.000E-03	4.427E+00	2.000E-03	9.810E-01	8.000E-03	7.945E+03	9.183E+01	...	...
	8.154E+00	2.000E-03	7.561E+00	3.000E-03	6.622E+00	5.000E-03	2.940E+00	3.400E-02	3.296E+03	6.177E+03	6.683E+03	8.697E+02
	8.048E+00	6.000E-03	6.613E+00	2.000E-03	5.777E+00	7.000E-03	2.145E+00	3.500E-02	5.854E+03	...	...	...
	2.760E+01	4.140E+00	4.499E+01	6.748E+00	6.267E+01	9.400E+00	...	...	...	...	...	...
	2.298E+01	3.447E+00	2.953E+01	4.430E+00	3.205E+01	4.808E+00	...	...	...	...	...	...
	9.893E+01	1.484E+01	1.515E+02	2.272E+01	1.872E+02	2.808E+01	8.494E+02	1.274E+02	...	...	...	...
	6.453E+01	9.679E+00	9.339E+01	1.401E+01	6.046E+01	9.069E+00	...	...	...	...	...	...
	1.341E+01	2.011E+00	2.509E+01	3.763E+00	2.886E+01	4.328E+00	...	...	...	...	...	...
	4.727E+00	7.090E-01	4.491E+00	6.736E-01	4.919E+00	7.378E-01	...	...	...	...	...	...
			160	160 err	250	250 err	350	350 err	500	500 err	1300	1300 err
			...	...	...	...	...	...	...	...	6.574E+01	1.223E+00
			...	...	...	...	...	...	...	...	6.160E+01	7.900E-01
			...	...	...	...	...	...	...	...	3.903E+01	4.480E-01
			...	...	...	...	...	...	...	...	...	...
			...	...	...	...	...	...	...	...	...	...
			...	...	...	...	...	...	...	...	...	...
			...	...	...	...	...	...	...	...	...	...
			...	...	...	...	...	...	...	...	...	...
			...	...	...	...	...	...	...	...	...	...

NOTE—Table 2 is published in its entirety in the machine-readable format. A portion is shown here for guidance regarding its form and content.

**Table 3.** SED-derived parameters for the 28 YSOs in the SMA-observed Region of G79.3+0.3

R.A. (degrees)	Dec (degrees)	SMA ID	<i>Spitzer</i> ID	YSO Class	Mass ( $M_{\odot}$ )	Luminosity ( $L_{\odot}$ )	Extinction ( $A_V$ ) (mag)
308.092102	40.338074	1	J203222.10+402017.1	1	5.77 ± 1.73	1543 ± 470	62.9 ± 18.6
308.119202	40.328213	4	J203228.61+401941.6	1	5.17 ± 1.55	815 ± 244	24.8 ± 7.4
308.096008	40.322975	5	J203223.04+401922.7	2	4.00 ± 1.20	37.6 ± 11.3	7.85 ± 2.35
308.085846	40.330597	–	J203220.60+401950.1	1	4.23 ± 1.27	268 ± 80	91.1 ± 27.3
308.092682	40.332169	–	J203222.25+401955.8	1	3.29 ± 0.99	29.1 ± 8.7	40.3 ± 12.1
308.116089	40.328426	–	J203227.86+401942.3	1	3.25 ± 0.97	34.7 ± 10.4	30.7 ± 9.2
308.088043	40.340446	–	J203221.13+402025.6	1	3.24 ± 0.97	96.6 ± 29.0	32.7 ± 9.8
308.083893	40.331524	–	J203220.14+401953.5	1	3.18 ± 0.95	122 ± 37	54.9 ± 16.5
308.088013	40.333580	–	J203221.13+402000.9	1	3.15 ± 0.94	67.7 ± 20.3	81.0 ± 24.3
308.115021	40.320698	–	J203227.61+401914.5	2	3.07 ± 0.92	15.6 ± 4.7	33.8 ± 10.1
308.095093	40.328014	–	J203222.82+401940.9	1	3.00 ± 0.90	32.5 ± 9.8	59.1 ± 17.7
308.079529	40.336517	–	J203219.09+402011.5	1	2.41 ± 0.72	9.62 ± 2.88	100 ± 30
308.072327	40.330471	–	J203217.36+401949.7	2	2.24 ± 0.67	25.2 ± 7.6	28.4 ± 8.5
308.095795	40.339264	–	J203222.99+402021.4	1	2.20 ± 0.66	24.0 ± 7.2	18.4 ± 5.5
308.087952	40.313370	–	J203221.11+401848.1	2	2.09 ± 0.63	4.56 ± 1.37	14.7 ± 4.4
308.074768	40.332897	–	J203217.95+401958.4	2	1.35 ± 0.41	9.41 ± 2.82	14.0 ± 4.2
308.111969	40.319542	–	J203226.87+401910.4	2	1.35 ± 0.41	9.41 ± 2.82	16.2 ± 4.9
308.079468	40.328423	–	J203219.07+401942.3	1	1.00 ± 0.30	5.96 ± 1.79	38.4 ± 11.5
308.108429	40.317829	–	J203226.02+401904.2	2	0.737 ± 0.221	3.44 ± 1.03	29.0 ± 8.7
308.086060	40.314732	–	J203220.65+401853.0	1	0.577 ± 0.173	3.93 ± 1.18	22.9 ± 6.9
308.084778	40.333744	–	J203220.34+402001.5	1	0.469 ± 0.141	0.803 ± 0.241	5.00 ± 1.50
308.098022	40.343136	–	J203223.52+402035.3	2	0.373 ± 0.112	1.29 ± 0.39	23.5 ± 7.0
308.122589	40.321468	–	J203229.42+401917.3	2	0.214 ± 0.064	0.719 ± 0.216	11.7 ± 3.5
308.113464	40.323074	–	J203227.23+401923.1	2	0.173 ± 0.052	1.27 ± 0.38	30.3 ± 9.1
308.078186	40.334187	–	J203218.76+402003.1	2	0.157 ± 0.047	0.691 ± 0.207	19.1 ± 5.7
308.077515	40.336700	–	J203218.61+402012.1	2	0.152 ± 0.046	0.250 ± 0.075	9.84 ± 2.95
308.073486	40.333916	–	J203217.64+402002.1	2	0.146 ± 0.044	1.23 ± 0.37	6.20 ± 1.86
308.084167	40.313576	–	J203220.20+401848.9	2	0.107 ± 0.032	0.115 ± 0.034	6.38 ± 1.91

input fluxes were too strongly constrained (Robitaille 2008). The  $\chi^2$  value for SMA object 1 is large, indicating a poor fit. These are a few reasons to only use the SED-derived parameters as first estimates, along with further reasons discussed in Section 4.2. A selection of the G79.3+0.3 object parameters is given in Table 3 with the uncertainty in each parameter set to  $\pm 30\%$  following Saral et al. (2017).

Figure 4 shows the spatial distribution of YSOs across G79.3+0.3 and its surrounding area, with the symbols showing their YSO class and mass. Within G79.3+0.3, the more massive objects tend to be near the center of the cloud and located close to each other. These more massive objects are almost entirely Class I objects, whereas the Class II objects are lower mass and are located on the outskirts of the covered area. The distribution is similar in the IRDC region seen on the right side of Figure 4, which is unsurprising given that the two regions are connected behind the foreground warm dust emission (Redman et al. 2003).

### 3.3. Molecular outflows seen in $^{12}\text{CO}$

To identify molecular outflows in G79.3+0.3, we examined the  $^{12}\text{CO}$  J=2-1 emission in various velocity bins across the region. The dominant CO emission feature in the images is the narrow linear structure at a position angle (PA) of  $100.4 \pm 0.4^\circ$ . This structure is seen in the blueshifted velocities from  $-12$  km s $^{-1}$  up to  $-50$  km s $^{-1}$ , and in the redshifted velocities from  $11$  km s $^{-1}$  up to  $45$  km s $^{-1}$ . This high-velocity CO emission traces a protostellar outflow from a young protostar in the region. Following Zhang et al. (2005), we integrate the blueshifted and redshifted CO emission to produce the outflow image shown in Figure 5. We estimate outflow parameters including its mass, energy, and momentum using the  $^{12}\text{CO}$  emission. The mass of the gas can be estimated from the column density,  $\bar{N}(\text{CO})$ . Following the formula in Garden

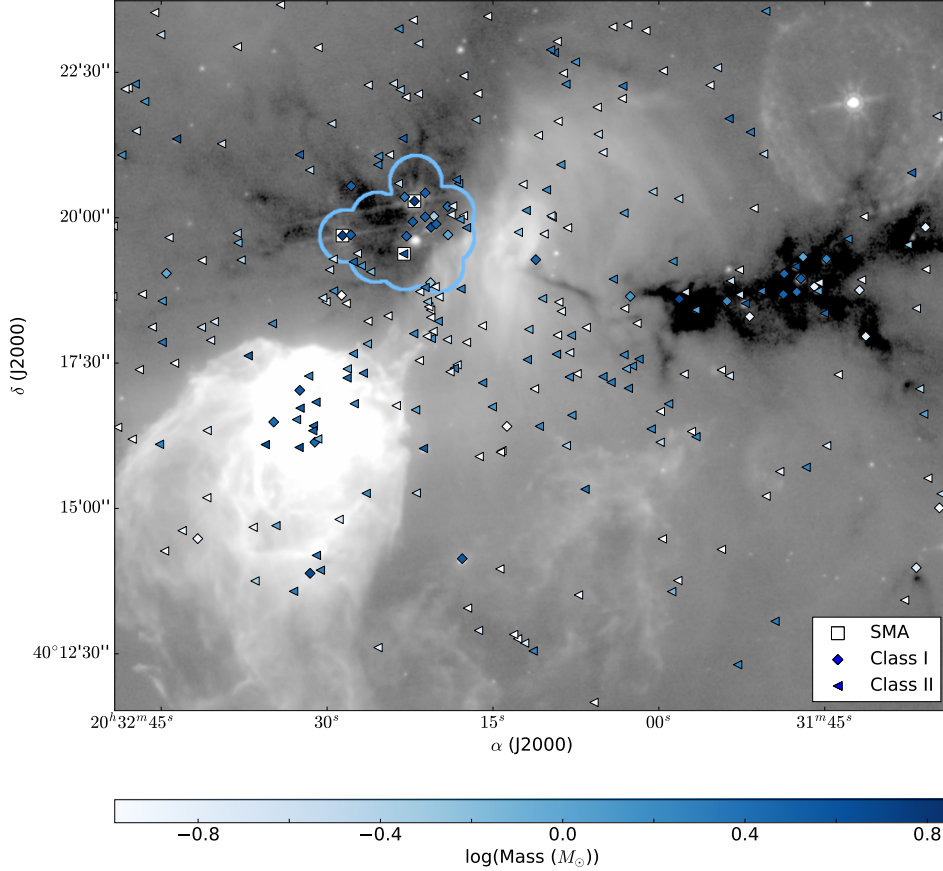


**Figure 4.** The spatial distribution of YSOs across G79.3+0.3 and its surrounding area. The region covered by our SMA data is outlined in blue near the upper left of the image. Class I YSOs are plotted as diamonds, Class II YSOs as triangles, and the symbols are shaded according to their mass derived from the SED fitting using the color scale shown below the image, with darker blue being higher mass. Each of the three SMA objects is highlighted with a white square. The background image is the  $8 \mu\text{m}$  *Spitzer* image, and the dark black regions are IRDCs.

et al. (1991), we find the column density from the equation:

$$\bar{N}(\text{CO}) = 4.34 \cdot 10^{13} \cdot \frac{1}{2} \exp(5.525/T_{ex}) \cdot \frac{(T_{ex} + 0.92)}{\exp(-11.1/T_{ex})} \int \frac{T_B \tau dv}{(1 - \exp(-\tau))}. \quad (1)$$

The integral is simplified by placing  $\bar{N}$  into the  $M_{gas}$  equation to obtain:

$$M_{gas} = 1.6 \cdot 10^{-7} \cdot \frac{1}{2} \exp(5.525/T_{ex}) \cdot \frac{(T_{ex} + 0.92)}{\exp(-11.1/T_{ex})} \cdot \frac{\bar{\tau}}{1 - \exp(-\bar{\tau})} \cdot \left[ \frac{\theta}{arcsec} \right]^2 \int T_B dv M_{\odot}. \quad (2)$$

This method uses estimates of the mean optical depth  $\bar{\tau}$  of CO, and the excitation temperature  $T_{ex}$ . We assume that CO is optically thin, and a typical  $T_{ex}$  of 20K.

The total outflow mass can be used to derive the outflow momentum  $P = M(\Delta v, \bar{\tau})|\bar{v}|$  and energy  $E = \frac{1}{2}M(\Delta v, \bar{\tau})\bar{v}^2$  for mean optical depth  $\bar{\tau}$ . We can combine these results with the dynamical timescale of the outflow  $t_{dyn}$  to find: the rate of

outflow mass  $\dot{M} = M/t_{dyn}$ ; the mechanical force  $F = P/t_{dyn}$ ; and the outflow luminosity  $L = E/t_{dyn}$  (Zhang et al. 2005). The dynamical timescale can in turn be found by taking the ratio of the maximum extent of the outflow and the maximum speed of the gas. In order to compare with the studies in the literature, we did not correct for the inclination angle of the outflow when estimating outflow parameters.

The  $^{12}\text{CO}$  emission that tracks the major outflow stemming from SMA object 3 is shown in Figure 5. The outflow parameters are given in Table 4. We estimated the spatial extent of the outflow using trigonometry, finding projected lengths  $L_R = 0.43$  pc and  $L_B = 0.94$  pc for the red- and blueshifted halves of the outflow, respectively. The actual extent of the outflow is likely larger, given that it is inclined towards us at some unknown angle.

## 4. DISCUSSION

### 4.1. SMA Continuum

The SMA objects 1, 4, and 5 can clearly be seen with the infrared instruments featured in Figure 2. It is possible that all three closely-placed SMA objects (1 through 3)



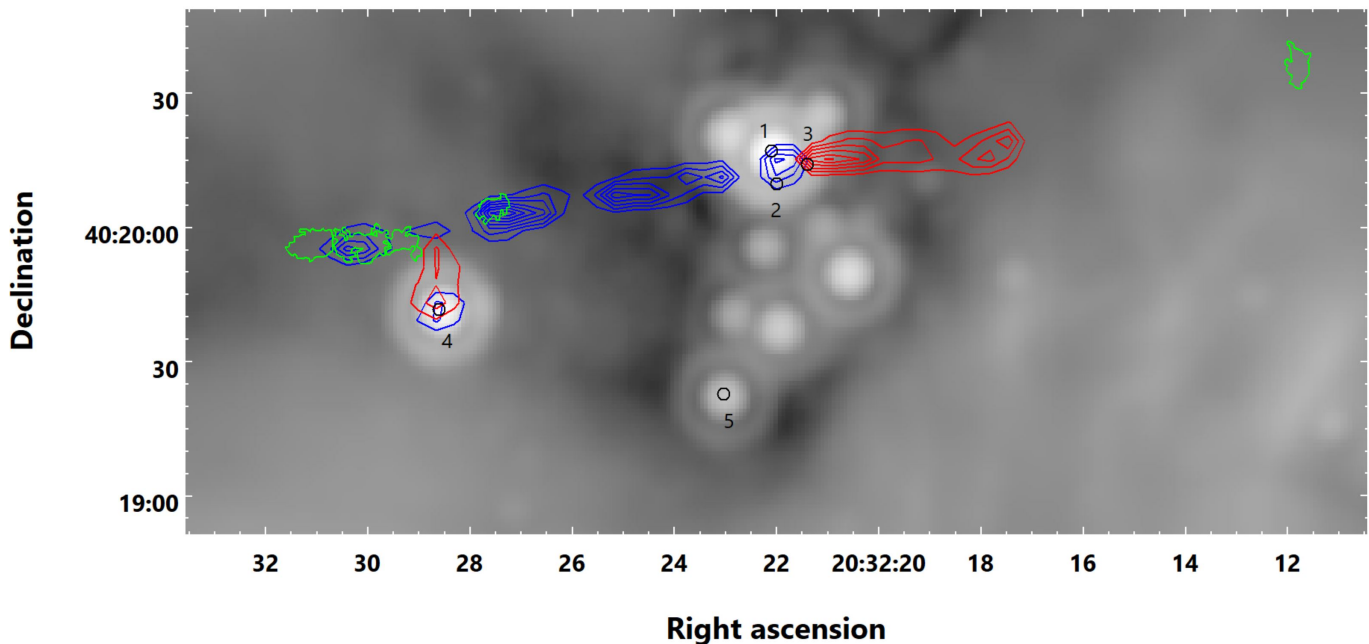


**Figure 5.**  $\text{H}_2$  and  $^{12}\text{CO}$  tracers of the large outflow from SMA object 3, plotted on the  $24\ \mu\text{m}$  *Spitzer* image. The  $^{12}\text{CO}$  emission is integrated over  $7.8$  to  $46.8\ \text{km s}^{-1}$  for the redshifted emission (red contours), and  $-31.2$  to  $-7.8\ \text{km s}^{-1}$  for the blueshifted emission (blue contours). The contours are spaced at  $7.8\ \text{Jy km s}^{-1}$  intervals. Green contours show the  $\text{H}_2$  emission from [Makin & Froebrich \(2018\)](#) as described in Section 4.3. The black markers labeled 1 through 5 show the locations of the five sources in our SMA  $1.3\ \text{mm}$  continuum image. The origin of the  $\text{H}_2$  and  $^{12}\text{CO}$  is consistent with SMA object 3 being the source of the outflow.

have significant emission in the *Herschel* bands, but were too poorly-resolved to be distinguished as individual objects. There is some indication that Source 1 is slightly extended in the direction of Object 3 at  $70$  and  $160\ \mu\text{m}$ . The dominant emission is still from Source 1 at  $160\ \mu\text{m}$ . However, at the  $1.3\ \text{mm}$  band Objects 2 and 3 are each more than twice as bright as Object 1, suggesting that it is likely that Objects 2 and 3 are deeply embedded in the cloud, and are at an earlier stage of evolution.

Our SMA continuum map is consistent with a previous observation of  $\text{G79.3+0.3}$  by [Redman et al. \(2003\)](#), who observed a portion of the IRDC at  $3\ \text{mm}$  using BIMA and resolved our SMA Objects 1 through 3 (their sources C, B, and A) and seem to have also detected SMA Object 5. Their image shows blueshifted  $\text{HCO}^+(1-0)$  line emission that is consistent with a strong outflow from Object 3, matching the outflow that is traced with the  $^{12}\text{CO}$  line emission from the SMA. The BIMA and SMA observations agree that Object 1 is the most massive star in  $\text{G79.3+0.3}$ . [Redman et al. \(2003\)](#) conclude that our SMA Object 1 will likely evolve into a B star on the main sequence and is too young to have disrupted the IRDC and triggered further star formation, but that this could happen over the next  $10^6$  years.

[Motte et al. \(2007, Object S37\)](#) reported a total mass of  $45\ M_{\odot}$  for SMA Objects 1, 2 and 3 based on the MOMBO data at the  $1.2\ \text{mm}$  band and a resolution of  $11''$ . The SMA observations have sufficient spatial resolution to distinguish

the compact cores. Therefore, the mass estimates in this paper are consistent with that reported in [Motte et al. \(2007\)](#).

SMA Objects 4, 5, and the grouping of 1 through 3 are roughly equidistant (the distances are: 1–4,  $0.70\ \text{pc}$ ; 4–5,  $0.58\ \text{pc}$ ; and 1–5,  $0.38\ \text{pc}$ ). This is similar to the massive IRDC 18223 reported by [Beuther et al. \(2015\)](#), which has twelve cores regularly spaced at  $0.40 \pm 0.18\ \text{pc}$  and peak separations varying between  $0.19\ \text{pc}$  and  $0.70\ \text{pc}$ , as well as to IRDC G28.34 ([Zhang et al. 2009](#)) with five regularly spaced cores. The similarity between the inter-core separations in IRDC 18223 and the inter-stellar separations in  $\text{G79.3+0.3}$  suggests that our five SMA objects were originally part of the same filamentary structure. This can be expanded upon further by considering SMA Objects 1 through 3, which are roughly equidistant with a separation of around  $0.069\ \text{pc}$ , and so were likely formed from a single massive gas structure that further fragmented into the three objects. The separations between our SMA objects are comparable to the Jeans length in  $\text{G79.3+0.3}$  of  $0.50\ \text{pc}$ , assuming values of gas density and kinetic temperature from [Carey et al. \(1998, Table 3\)](#). This similarity between inter-star distance and Jeans length is as expected and has been seen in many other clouds (e.g. [Teixeira et al. 2006](#); [Feng et al. 2016](#)).

#### 4.2. SEDs and Parameters

The SEDs of the three SMA objects are reasonable for a first estimate of the object parameters, since the inclusion of

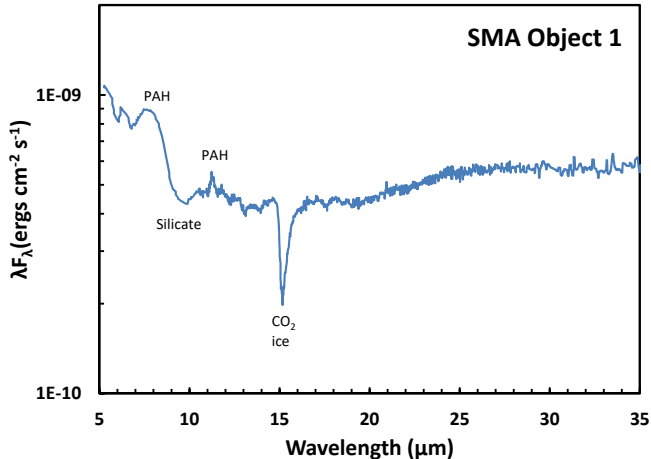


**Figure 6.** The spectrum of SMA object 1, adapted from Segura-Cox et al. (2011, Object CYGXS37). This spectrum was measured using *Spitzer*’s InfraRed Spectrograph (IRS). There are emission features due to Polycyclic Aromatic Hydrocarbons (PAHs) at  $\sim 8$  and  $11 \mu\text{m}$ , and absorption features due to  $\text{H}_2\text{O}$  ice at  $6 \mu\text{m}$ , silicates at  $\sim 10 \mu\text{m}$ , and  $\text{CO}_2$  ice at  $\sim 15 \mu\text{m}$ .

SMA data gives model SEDs consistent with their previous classifications based on *Spitzer* data.

Segura-Cox et al. (2011) reduced a spectrum for SMA Object 1 from data obtained in *Spitzer* project ID 50045 (Fazio et al. 2008), shown in Figure 6. This covers the  $5 \mu\text{m} \leq \lambda \leq 34 \mu\text{m}$  range in much higher detail than our SED in Figure 3. Both the spectrum and the best-fit SED show silicate absorption at  $10 \mu\text{m}$ , which is consistent with the object being a Class I YSO. Notably, the spectrum shows features usually seen in massive YSOs, including strong  $\text{CO}_2$  ice absorption at  $15.4 \mu\text{m}$  and  $\text{H}_2\text{O}$  ice absorption near  $6 \mu\text{m}$  (An et al. 2009). The  $15.4 \mu\text{m}$  absorption is caused by mixing of  $\text{CO}_2$  and  $\text{CH}_3\text{OH}$ , which are abundant in massive YSOs (An et al. 2011). There was some weak  $\text{CH}_3\text{OH}$  line emission visible in our SMA spectra across G79.3+0.3, but the signal-to-noise ratio was too poor to map it across the region.

It is important to consider the SED-derived parameters as first estimates, rather than the true physical values of the objects. We are using large uncertainties of  $\pm 30\%$ , and the models make potentially false assumptions of the objects, such as assuming that the YSO envelope is in free-fall, that the objects all have solar metallicity, and that the disc and envelope gas-to-dust ratios are 100 (Robitaille et al. 2006).

SMA Objects 1 and 4 are the two most massive and luminous objects in this region of G79.3+0.3, and also have the highest extinction. Their high luminosities are consistent with being Class I YSOs that will likely become massive stars, as they are already near the  $8M_\odot$  limit and are still actively accreting mass. Objects 1 and 4 also have high extinction values compared with the expected values for Cygnus-X of

$5 \leq A_v \leq 10$ , which indicates that the objects are deeply embedded in the IRDC. On the other hand, Object 5 has very low extinction and therefore might be in the foreground of the dark cloud.

The area surrounding G79.3+0.3 shows many Class II objects of varying mass, few of which appear significantly clustered. There is a patch of closely-placed Class II objects just below our IRDC at approximately  $20^{\text{h}}32^{\text{m}}20^{\text{s}}$ ,  $40^\circ 18'00''$  (J2000.0). These objects could be part of the same cloud if it has been obscured by foreground emission, as in the case of the connection between G79.3+0.3 and the nearby IRDC seen in Figure 4. For the most part, the Class II objects are lower-mass and more spatially distributed than the Class I objects in this region of Cygnus-X.

#### 4.3. Outflow from SMA Object 3

The outflow parameters we derived have similar magnitudes to the sample of 39 objects with outflows in Zhang et al. (2005).

The total mass of the outflow is  $0.83 M_\odot$ , consistent with the sample of six outflows given in Lee et al. (2002, Table 3), which cover a range  $0.01 - 1.00 M_\odot$ . It is also twice as massive as any of the six nearby outflows in DR21 found by Hawley (2012, Table 4), despite those six outflows being ejected from much more massive YSOs. The outflow could be so massive and energetic because there is no other outflow detected nearby that could disrupt the flow of material or otherwise interfere with the YSO’s accretion process.

Other NIR images in the region surrounding G79.3+0.3 have revealed  $\text{H}_2$  emission corresponding to the outflow from SMA Object 3, that lies further out from the star than the  $^{12}\text{CO}$  emission (Makin & Froebrich 2018; Davis et al. 2010, “Catalogue of Molecular Hydrogen Emission-Line Objects (MHOs) in Outflows from Young Stars” object MHO 3597). The MHO catalog identifies the source of the outflow as J203222.10+402017.06 (our SMA object 1) (Kryukova et al. 2014), but our SMA observations reveal the true source to be the newly-identified SMA Object 3 (Figure 5). The  $\text{H}_2$  emission extends just beyond the furthest extent of the blueshifted lobe, and about the same distance in the redshifted direction. The SMA field observed ends about halfway to the  $\text{H}_2$  lobe in the redshifted direction, so we cannot tell if the redshifted  $^{12}\text{CO}$  emission extends a similar distance.

**Table 4.** Estimates of the Parameters for SMA Object 3 Outflow

Parameter	Redshifted lobe	Blueshifted lobe
Mass		

Table 4 continued

Table 4 (continued)

Parameter	Redshifted lobe	Blueshifted lobe
$(M_{\odot})$	0.37	0.46
Momentum		
$(M_{\odot} \text{ km s}^{-1})$	10.5	14.0
Energy		
$(M_{\odot} (\text{km s}^{-1})^2)$	163	221
Extent		
(pc)	0.43	0.94
Dynamical timescale		
(kyr)	10.5	23.0
Mass rate		
$(10^{-13} \cdot M_{\odot} \text{ s}^{-1})$	11.2	6.34
$(10^{-5} \cdot M_{\odot} \text{ yr}^{-1})$	3.53	2.00
Mechanical Force		
$(10^{-11} \cdot M_{\odot} \text{ km s}^{-2})$	3.17	1.93
Luminosity		
$(10^{-10} \cdot M_{\odot} (\text{km s}^{-1})^2 \text{ s}^{-1})$	4.91	3.05
$(10^{26} \cdot \text{ergs})$	9.76	6.06

For all we can find out about the outflow from Object 3, we cannot determine much about the central object itself. Object 3 has no previous detections in our catalogs, and so we could not fit a model SED and estimate the physical properties of this object.

## 5. CONCLUSIONS

We have produced a 1.3 mm continuum image of the IRDC G79.3+0.3 using the SMA. The image shows that this region of the IRDC contains five YSOs in an early stage of formation, one of which has a massive collimated  $^{12}\text{CO}$  outflow. The regular spacing of the objects hints at the fragmentation scale of the cloud being  $\sim 0.76$  pc.

We have estimated the properties of the YSOs using model SED fitting. In all cases, the slopes of the model SEDs are consistent with the objects' YSO classifications based on

color-color and color-magnitude diagrams using the near- and mid-IR data. The model SEDs for the three SMA objects 1, 4, and 5 returned masses in the range of  $4 - 6 M_{\odot}$ . This is consistent with their being massive YSOs, and in fact they are the most massive and luminous of the YSOs we identified in this region of G79.3+0.3.

We have identified an enormous  $^{12}\text{CO}$  outflow from SMA object 3. The outflow extent is at least 0.43 pc and 0.94 pc in the redshifted and blueshifted lobes respectively. The presence of this outflow is consistent with Object 3 being a protostar, and is also supported by the outflow parameters being of similar magnitude to parameters of massive outflows from other studies. The total mass of the outflow is 0.37 and  $0.46 M_{\odot}$  and total momentum is 10.5 and  $14.0 M_{\odot} \text{ km s}^{-1}$  in the red and blue lobes, respectively.

## ACKNOWLEDGEMENTS

The authors wish to recognize and acknowledge the very significant cultural role and reverence that the summit of Maunakea has always had within the indigenous Hawaiian community. We are most fortunate to have the opportunity to conduct observations from this mountain.

This work is based in part on observations made with the *Spitzer* Space Telescope, which is operated by the Jet Propulsion Laboratory, California Institute of Technology under a contract with NASA. Support for this work was provided by NASA through an award issued by JPL/Caltech.

*Herschel* is an ESA space observatory with science instruments provided by European-led Principal Investigator consortia and with important participation from NASA.

This publication makes use of data products from the Two Micron All Sky Survey, which is a joint project of the University of Massachusetts and the Infrared Processing and Analysis Center/California Institute of Technology, funded by the National Aeronautics and Space Administration and the National Science Foundation.

This work is based in part on data obtained as part of the UKIRT Infrared Deep Sky Survey.

The authors wish to thank S.V. Makin for providing the data on  $\text{H}_2$  emission in the G79.3+0.3 region. The authors thank the anonymous referee for their useful comments that have improved our paper.

## REFERENCES

- An, D., Ramírez, S. V., Sellgren, K., et al. 2009, *ApJL*, 702, L128  
—, 2011, *ApJ*, 736, 133  
Beerer, I. M., Koenig, X. P., Hora, J. L., et al. 2010, *ApJ*, 720, 679  
Beuther, H., Ragan, S. E., Johnston, K., et al. 2015, *A&A*, 584, A67  
Beuther, H., Schilke, P., Sridharan, T. K., et al. 2002, *A&A*, 383, 892  
Calahan, J., Hora, J. L., & Siraj, A. in prep.  
Carey, S. J., Clark, F. O., Egan, M. P., et al. 1998, *ApJ*, 508, 721  
Cyganowski, C. J., Whitney, B. A., Holden, E., et al. 2008, *AJ*, 136, 2391  
Davis, C. J., Gell, R., Khanzadyan, T., Smith, M. D., & Jenness, T. 2010, *A&A*, 511, A24  
Dye, S., Warren, S. J., Hambly, N. C., et al. 2006, *MNRAS*, 372, 1227

- Fazio, G., Adams, J., Allen, L., et al. 2008, Spectra of Massive Young Stars in the Cygnus-X Complex, Spitzer Proposal, ,
- Fazio, G. G., Hora, J. L., Allen, L. E., et al. 2004, *ApJS*, 154, 10
- Feng, S., Beuther, H., Zhang, Q., et al. 2016, *A&A*, 592, A21
- Garden, R. P., Hayashi, M., Hasegawa, T., Gatley, I., & Kaifu, N. 1991, *ApJ*, 374, 540
- Gutermuth, R. A., Myers, P. C., Megeath, S. T., et al. 2008, *ApJ*, 674, 336
- Hawley, W. 2012, Master's thesis, Harvard College
- Ho, P. T. P., Moran, J. M., & Lo, K. Y. 2004, *ApJL*, 616, L1
- Hora, J. L., Bontemps, S., Megeath, T., et al. 2011, The CygnusX Legacy Project Data Description: Delivery 1, <http://irsa.ipac.caltech.edu/data/SPITZER/Cygnus-X/docs/CygnusDataDelivery1.pdf>, ,
- Kirk, J. 2014, Master's thesis, University of Southampton
- Kryukova, E., Megeath, S. T., Hora, J. L., et al. 2014, *AJ*, 148, 11
- Lee, C.-F., Mundy, L. G., Stone, J. M., & Ostriker, E. C. 2002, *ApJ*, 576, 294
- Makin, S. V., & Froebrich, D. 2018, *ApJS*, 234, 8
- Marton, G., Calzoletti, L., Perez Garcia, A. M., et al. 2017, *ArXiv e-prints*, arXiv:1705.05693
- McKee, C. F., & Ostriker, E. C. 2007, *ARA&A*, 45, 565
- McMullin, J. P., Waters, B., Schiebel, D., Young, W., & Golap, K. 2007, in *Astronomical Society of the Pacific Conference Series*, Vol. 376, *Astronomical Data Analysis Software and Systems XVI*, ed. R. A. Shaw, F. Hill, & D. J. Bell, 127
- Motte, F., Bontemps, S., & Louvet, F. 2017, *ArXiv e-prints*, arXiv:1706.00118
- Motte, F., Bontemps, S., Schilke, P., et al. 2007, *A&A*, 476, 1243
- Palau, A., Ho, P. T. P., Zhang, Q., et al. 2006, *ApJL*, 636, L137
- Peretto, N., & Fuller, G. A. 2010, *ApJ*, 723, 555
- Ragan, S., Henning, T., Krause, O., et al. 2012, *A&A*, 547, A49
- Rathborne, J. M., Jackson, J. M., & Simon, R. 2006, *ApJ*, 641, 389
- Redman, R. O., Feldman, P. A., Wyrowski, F., et al. 2003, *ApJ*, 586, 1127
- Rieke, G. H., Young, E. T., Engelbracht, C. W., et al. 2004, *ApJS*, 154, 25
- Rivera-Gálvez, S., Román-Zúñiga, C. G., Jiménez-Bailón, E., et al. 2015, *AJ*, 150, 191
- Rizzo, J. R., Palau, A., Jiménez-Esteban, F., & Henkel, C. 2014, *A&A*, 564, A21
- Robitaille, T. P. 2008, in *Astronomical Society of the Pacific Conference Series*, Vol. 387, *Massive Star Formation: Observations Confront Theory*, ed. H. Beuther, H. Linz, & T. Henning, 290
- Robitaille, T. P. 2013, *Python SED Fitter documentation*, <https://sedfitter.readthedocs.io/en/stable/>, ,
- Robitaille, T. P., Whitney, B. A., Indebetouw, R., & Wood, K. 2007, *ApJS*, 169, 328
- Robitaille, T. P., Whitney, B. A., Indebetouw, R., Wood, K., & Denzmore, P. 2006, *ApJS*, 167, 256
- Rygl, K. L. J., Brunthaler, A., Sanna, A., et al. 2012, *A&A*, 539, A79
- Saral, G., Hora, J. L., Audard, M., et al. 2017, *The Astrophysical Journal*, 839, 108
- Sault, R. J., Teuben, P. J., & Wright, M. C. H. 1995, in *Astronomical Society of the Pacific Conference Series*, Vol. 77, *Astronomical Data Analysis Software and Systems IV*, ed. R. A. Shaw, H. E. Payne, & J. J. E. Hayes, 433
- Schneider, N., Bontemps, S., Simon, R., et al. 2006, *A&A*, 458, 855
- Schneider, N., Bontemps, S., Motte, F., et al. 2016, *A&A*, 591, A40
- Segura-Cox, D., Hora, J. L., Smith, H. A., et al. 2011, in *Bulletin of the American Astronomical Society*, Vol. 43, *American Astronomical Society Meeting Abstracts #217*, 340.13
- Shang, H., Li, Z.-Y., & Hirano, N. 2007, *Protostars and Planets V*, 261
- Shu, F. H., Najita, J. R., Shang, H., & Li, Z.-Y. 2000, *Protostars and Planets IV*, 789
- Skrutskie, M. F., Cutri, R. M., Stiening, R., et al. 2006, *AJ*, 131, 1163
- Tan, J. C., Beltrán, M. T., Caselli, P., et al. 2014, *Protostars and Planets VI*, 149
- Teixeira, P. S., Lada, C. J., Young, E. T., et al. 2006, *ApJL*, 636, L45
- Umana, G., Buemi, C. S., Trigilio, C., et al. 2011, *ApJL*, 739, L11
- Wang, K., Zhang, Q., Wu, Y., Li, H.-b., & Zhang, H. 2012, *ApJL*, 745, L30
- Wang, K., Zhang, Q., Testi, L., et al. 2014, *MNRAS*, 439, 3275
- Wang, K.-S., Bourke, T. L., Hogerheijde, M. R., et al. 2013, *A&A*, 558, A69
- Wang, Y., Zhang, Q., Rathborne, J. M., Jackson, J., & Wu, Y. 2006, *ApJL*, 651, L125
- Welch, W. J. 1988, in *Astrophysics and Space Science Library*, Vol. 147, *Millimetre and Submillimetre Astronomy*, ed. R. D. Wolstencroft & W. B. Burton (Kluwer Academic Publishers), 95–116
- Werner, M. W., Roellig, T. L., Low, F. J., et al. 2004, *ApJS*, 154, 1
- Wright, N. J., Drew, J. E., & Mohr-Smith, M. 2015, *MNRAS*, 449, 741
- Zhang, Q., Ho, P. T. P., Wright, M. C. H., & Wilner, D. J. 1995, *ApJL*, 451, L71+
- Zhang, Q., Hunter, T. R., Brand, J., et al. 2005, *ApJ*, 625, 864
- . 2001, *ApJL*, 552, L167
- Zhang, Q., & Wang, K. 2011, *ApJ*, 733, 26
- Zhang, Q., Wang, Y., Pillai, T., & Rathborne, J. 2009, *ApJ*, 696, 268
- Zinnecker, H., & Yorke, H. W. 2007, *ARA&A*, 45, 481

*Software:* MIR (<https://github.com/qi-molecules/sma-mir>), CASA (McMullin et al. 2007), MIRIAD (Sault et al. 1995), SEDFitter (v1.0 Robitaille et al. 2007)